The Astrophysical Journal, 994:3 (13pp), 2025 November 20 https://doi.org/10.3847/1538-4357/ae0992

An Intense Geomagnetic Storm Originated from Stealth Coronal Mass Ejection: Remote and In Situ Observations by Near Radially Aligned Spacecraft

P. Vemareddy[1] and K. Selva Bharathi[1,2]
[1] Indian Institute of Astrophysics, II Block, Koramangala, Bengaluru-560 034, India; vemareddy@iiap.res.in, selvabharathik@students.iisertirupati.ac.in
[2] Indian Institute of Science Education and Research, Tirupati-517 507, India

Received 2025 July 10; revised 2025 September 5; accepted 2025 September 11; published 2025 November 11

Abstract

We investigate the solar origin and heliospheric evolution of an intense geomagnetic storm that occurred on 2023 March 23–24. Despite multiple candidate coronal mass ejections (CMEs) observed between March 19 and 21, a weak CME detected on March 19 at 18:00 UT was identified as the cause, originating from the eruption of a longitudinal-filament channel near the center of the Sun. The channel underwent a smooth transition to the eruption phase without detectable low-coronal signatures. Wide-angle heliospheric imaging revealed asymmetric expansion and acceleration by solar wind drag, achieving an average CME velocity of $\approx$640 km s^{-1}. The radial evolution of the interplanetary coronal mass ejection (ICME) was analyzed by three spacecraft in close radial alignment. Arrival times and propagation speeds were consistent across spacecraft, with a 21 hr delay between STEREO-A (STA) and WIND attributed to solar rotation and longitudinal separation. The ICME exhibits magnetic cloud (MC) signatures characterized by right-handed helicity, enhanced density at all three spacecraft. The MC underwent expansion (radial-size increases from 0.08 au at SolO to 0.18 au at STA), a decrease in magnetic field strength with distance; $B_{av} \propto R_H^{-1.97}$ (SolO-STA) and $B_{av} \propto R_H^{-1.53}$ (SolO-WIND). The MC axis is inclined with the ecliptic at $-69°$ at SolO, $-25°$ at STA, and $-34°$ at WIND, indicating rotation during heliospheric transit. Importantly, the storm's main phase leads to a peak intensity (SYM-H$= -169$ nT) occurring at 24/02:40 UT, followed by a second peak (SYM-H $= -170$ nT) at 24/05:20 UT due to density enhancement toward MC's tail. The study emphasizes the significant geoeffectiveness of weak, stealth CMEs with southward Bz and density enhancements.

Unified Astronomy Thesaurus concepts: Solar coronal mass ejections (310); Solar-terrestrial interactions (1473); Heliosphere (711); Solar storm (1526)

1. Introduction

Geomagnetic storms are major disturbances in the Earth's magnetosphere, which are measured with the Disturbance Storm Time (Dst) index. Based on the peak Dst index, the storms are classified as moderate ($-100 \leqslant \mathrm{Dst} \leqslant -50$ nT), intense ($-250 \leqslant \mathrm{Dst} < -100$ nT), and superstorms ($\mathrm{Dst} \leqslant -250$ nT) (W. D. Gonzalez et al. 1994). These storms are known to be driven by solar wind structures such as interplanetary coronal mass ejections (ICMEs), and/or corotating interaction regions that possess a strong southward magnetic field component (J. T. Gosling et al. 1991; W. D. Gonzalez et al. 1999). During the storm, the IMF field reconnects with Earth's magnetic field, permitting the solar energetic particles to penetrate the Earth's atmosphere. Severe storms can lead to considerable harm, including widespread power failures from grid disruptions, damage to satellites and instruments from surface charging, interference with satellite navigation and radio communications, and major health threats to astronauts (E. J. Oughton et al. 2017). Thus, from the perspective of space weather and space-dependent technology, studying the solar origins and the impact of the geomagnetic storms has been important scientific research.

According to several reports, the most severe storms are triggered by powerful CMEs that come from the vicinity of the solar disk center (R. A. Howard et al. 1982; N. Gopalswamy et al. 2005). To understand the solar origins of a geomagnetic storm, one must investigate (i) the in situ magnetic field and plasma measurements for ICME signatures, (ii) the near-Sun imaging observations of its solar counterpart, namely, the CME from the previous 3–4 days, and (iii) the CME's source region on the solar disk. Using remote sensing data from SoHO (G. E. Brueckner et al. 1995), STEREO (M. L. Kaiser et al. 2008), and Solar Dynamics Observatory (SDO; W. D. Pesnell et al. 2012), numerous studies have indicated that white-light observations of CMEs are associated with solar disk features like filament or prominence structures (e.g., D. F. Webb & A. J. Hundhausen 1987; N. Gopalswamy et al. 2003; P. Vemareddy et al. 2012, 2017; P. Vemareddy & M. S. Ibrahim 2024), X-ray sigmoids (e.g., R. C. Canfield et al. 1999; N. Vasantharaju et al. 2019), and extreme ultraviolet (EUV) hot channels (e.g., X. Cheng et al. 2013; P. Vemareddy & J. Zhang 2014; P. Vemareddy et al. 2022). The appearance of these features is typically accompanied by a solar flare classified as GOES C, M, or X. Based on these observations, the solar sources of a geomagnetic storm are usually recognized by low coronal signatures (LCS) like filament/prominence eruptions, coronal dimming, posteruption arcades, flare ribbons, etc.

The study by J. Zhang et al. (2007) found that 11% of the 88 intense geomagnetic storms examined showed no eruptive signatures on the solar disk. This indicates that some CMEs can generate significant geoeffects without any obvious large-scale structures (LCS) associated with them. Furthermore, a study by I. G. Richardson & H. V. Cane (2010) on ICMEs revealed that there are solar counterparts for several ICMEs that do not have identifiable solar sources. The CMEs that are characterized by weak or absent LCS are referred to as "stealth" CMEs. It is generally understood that stealth CMEs are not linked to filament or sigmoid eruptions and primarily originate from quiet regions of the Sun, which feature relatively complex yet weak magnetic field distributions (A. A. Pevtsov et al. 2012). These CMEs typically produce quiet eruptions that have speeds at the lower end of the spectrum ($<300\,\mathrm{km\,s^{-1}}$). However, high-cadence, high-resolution EUV observations, complemented by advanced image-processing techniques, can detect faint LCS from these CMEs (N. Alzate & H. Morgan 2017).

The first observation of a stealth coronal mass ejection (CME) was made in 2008 June (E. Robbrecht et al. 2009). In situ parameters recorded by STEREO-B at a distance of 1 au revealed a classical magnetic flux rope (FR) structure. Notably, this CME did not originate from any active region, as traced back to its source. Instead, it emerged from a quiet area of the Sun with no prominent disk counterparts (LCS) and appeared extremely faint in coronagraph observations. All subsequent stealth CMEs observed since this event have exhibited the characteristic FR structure (J. O'Kane et al. 2021). Given the substantial evidence from detailed in situ observations that these CMEs can cause significant geomagnetic disturbances (N. V. Nitta & T. Mulligan 2017; N. V. Nitta et al. 2021), it is essential to investigate stealth CMEs and their evolution through the heliosphere for accurate geomagnetic storm forecasts. A thorough qualitative observational analysis should be conducted to study their origins, heliospheric propagation, and in situ characteristics.

Stealth CMEs have been associated with driving intense geomagnetic storms, and their low detectability in near-Sun observations can lead to inaccurate predictions. Effective storm forecasting requires knowledge of the CME's speed at 0.1 au and the precise location of its source region on the Sun. In this article, we examine an intense geomagnetic storm that arose from a stealth CME originating near the solar disk center. The recorded geomagnetic storm occurred on 2023 March 23–24, and was classified as intense, with a peak Dst of –163 nT. Importantly, in addition to remote observations, the Solar Orbiter (SolO) was in close radial alignment with STEREO-A (STA) and near-Earth spacecraft. This alignment enabled us to assess the radial evolution of the CME at heliocentric distances of 0.5 and 0.966 au, along with WIND measurements at L1. The first magnetometer observations from SolO recorded a stealth CME at 0.8 au, alongside measurements from Wind at 1 au and BepiColombo (E. E. Davies et al. 2021; J. O'Kane et al. 2021). The recent launch of space missions like SolO, BepiColombo, and the Parker Solar Probe (PSP) has made multipoint observations of ICMEs frequent, improving our understanding of their evolution in the heliosphere (E. E. Davies et al. 2020; N. Lugaz et al. 2022; C. Möstl et al. 2022). An overview of the in situ observations of the storm is presented in Section 2, while Section 3 discusses the solar source CME and its source region. Observations of the CME's heliospheric propagation are detailed in Section 4. A detailed analysis of in situ observations from radially aligned spacecraft is given in Section 5. Conclusions from this study, with a brief discussion, are furnished in Section 6.

2. Geomagnetic Storm During 2023 March 23–24 and Near-Earth In Situ Observations

A geomagnetic storm with a Dst value peaking at –163 nT occurred during 2023 March 23–24. Figure 1 plots the in situ measurements of magnetic field and plasma parameters from WIND, and Dst and Kp indices from NOAA. While B_{Tot} is increasing gradually from background solar wind values, the Bz field is negative and exhibits fluctuations during 07:30–18:00 UT on March 23, which is regarded as the sheath region. Following this, the Bz rotates from negative to positive values while B_{Tot} continues at 20 nT with little variation until 07:30 UT on March 24. These are the typical characteristics of ICME containing a magnetic cloud (MC). The MC leading and trailing edges have a clear distinction of plasma and magnetic field characteristics, based on which the MC interval is defined from 18:00 UT on March 23 to 07:30 UT on March 24. The MC structure has low proton density, proton β, and temperature compared to its pre- and postpassage of the spacecraft, as seen in Figures 1(b)–(c). During this event, the background solar wind velocity (V_{sw}) was reportedly higher than $500\,\mathrm{km\,s^{-1}}$, since 14:30 UT on March 21, followed by a lower speed during ICME duration; as a result, there is no shock observed. The MC interval has decreased V_{sw} from 480 to $430\,\mathrm{km\,s^{-1}}$, indicating the expansion of the MC (FR), which corresponds to an expansion speed of $25\,\mathrm{km\,s^{-1}}$.

From the magnetic field components, the elevation ($\theta = \sin^{-1}(B_z/B_{\mathrm{Tot}})$) and azimuthal ($\phi = \tan^{-1}(B_y/B_x)$) angles are derived and plotted in Figure 1(d). The θ and ϕ refer to the orientation of the magnetic field vector in the GSE reference frame. The MC leading edge (LE) is highly inclined to the ecliptic at $\theta = -80°$ (south), which then rotates to the ecliptic plane while the azimuth ϕ varies from 125° (west) to 240° (east). Therefore, the MC structure is an SWN configuration with right-handed (positive) magnetic helicity (V. Bothmer & R. Schwenn 1998; T. Mulligan et al. 1998).

Typically, the storm's onset to the main phase corresponds well with the increased southward (Bz) magnetic field; that said, the peak of Bz is cotemporal with the peak of Dst within 2 hr of difference (P. Vemareddy 2024). Surprisingly, in this event, the Bz field (magnitude) decreases during the main phase as the Dst progresses to its peak at 24/03:00 UT, and the Bz was –9.6 nT, half of its peak value. A key point for this unusually intense storm probably lies with the role of proton density, which is increasing from its lower value toward the MC's trailing edge. MCs with trailing density enhancements were observed in a few reports and are suggested to strengthen the storm (F. R. Fenrich & J. G. Luhmann 1998; S. K. Bisoi et al. 2016; N. Gopalswamy et al. 2022).

The storm was classified as a G4-intense on the NOAA scale as the Kp index reached a maximum of 8. Ionospheric disturbances were observed over the European sectors as studied by G. Nykiel et al. (2024), along with disturbances of the GPS/GLONASS signals over the city of Apatity in Russia as studied by V. B. Belakhovsky et al. (2024). The storm produced auroras over the USA, extending up to New Mexico and other mid-latitude parts of the world. It was reported that Rocket Lab delayed its launch process by 90 minutes after assessing the effects of the GMS.

Figure 2 shows the locations of the Sun-observing spacecraft in the Heliocentric Earth Ecliptic system in the inner heliosphere on 2023 March 21. SolO was located at 0.5 au heliocentric distance from the Sun, and is separated by 17.°5

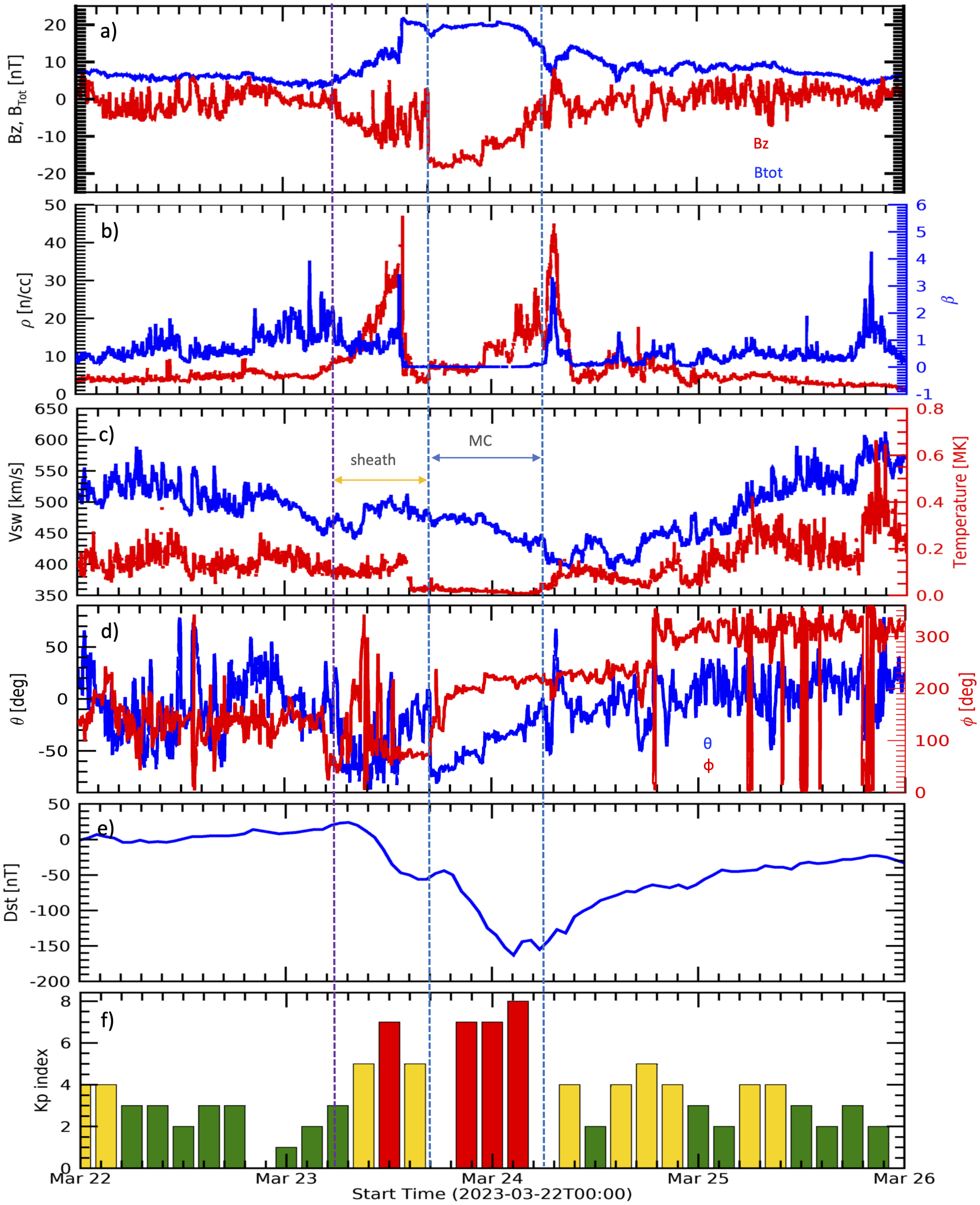

Figure 1. An intense geomagnetic storm during 2023 March 23–24 and the in situ observations. (a) The Bz- and B_{Tot}-components of the magnetic field observed by the WIND spacecraft. (b) The velocity and the proton density of the ICME. The purple dashed vertical line indicates the ICME arrival time (23/07:30 UT), and the blue vertical lines represent the MC interval (23/18:00–24/17:30 UT). (c) The proton density and proton β. Note the low density and β during the MC interval. (c) Solar wind velocity and temperature. (d) elevation (θ) and azimuthal (ϕ) angles of the magnetic field vector in the GSE frame. (e) A time-varying Dst index showing the storm commencing at 23/07:30 UT. The main phase of the storm progressed to a peak value of –163 nT on March 24 at 03:00 UT. (f) Histogram of the Kp index. The green, yellow, and red bars represent the index values 0–3, 3–6, and 6–9, respectively. During the storm's main phase, the Kp index values reached eight, referring to a powerful geomagnetic storm of G4 severity by space-weather classification.

from the Sun–Earth line; WIND was at the L1 point along the Sun–Earth line. STA was 0.966 au away from the Sun and had an angular separation of 11.°9 from the Sun–Earth line. In addition to the L1 point, the small angular separation of two spacecraft facilitates the study of the radial and longitudinal variation of magnetic and plasma in the ICME. The radial propagation of that ICME would mean it would encounter SolO, STA, and WIND. So, we took advantage of this rare radial lineup of spacecraft and compared the ICME in situ parameters, FR configuration, and its radial evolution at 0.5, 0.966 au, and at the L1 point.

3. Solar Source of the Geomagnetic Storm

To identify the solar source of this storm, the remote sensing multiwavelength images captured by SDO, STA, and SOHO are searched for an on-disk eruption and its associated halo white-light CME in the past 4 days. We have examined the running difference (RD) white-light images available at the

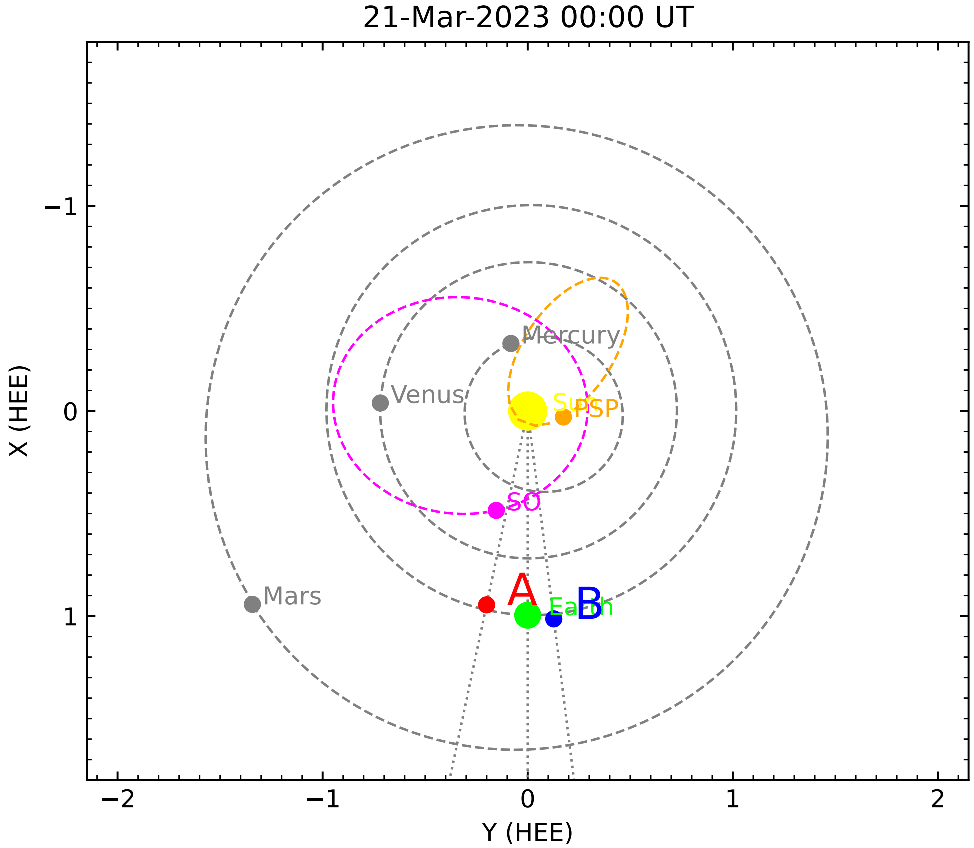

Figure 2. The locations of the different spacecraft on 2023 March 21 00:00 UT are used in the study. SO (pink) is the Solar Orbiter in its flyby orbit. A (red) and B (blue) refer to STEREO-A and STEREO-B. PSP (orange) near the Sun is the Parker Solar Probe in its orbit with the Earth (green) at 1 au distance from the Sun. And the Sun (yellow) at [0, 0] coordinates.

CDAW CME catalog[3] (S. Yashiro et al. 2004). Few potential CMEs occurred on March 19–20; however, their arrival at L1 was ruled out as these CMEs are not halo, and their source region was located near the limb. After a careful examination of RD images, a faint, slow-moving CME was identified in the Large Angle and Spectrometric Coronagraph (LASCO)/C2, STA/COR2 observations on March 19 at around 19:00 UT (19/19:00 UT for brevity) and used the same in the rest of this paper. Figure 3 shows the CME in the RD images from LASCO/C2 and STA/COR2. In C2 images, the CME first appeared at around 19/18:00 UT in the southern part as a narrow structure propagating southward, with a position angle slightly greater than 200°. As the CME moved out radially, its extent was also seen in the solar north. Mostly, the southern LE was traceable during the first 2 hr of the CME's expansion. Starting from 22:30 UT, a faint structure of this CME appears in the north. In the subsequent LASCO/C2 RD images, as seen in Figure 3, the northern edge of the CME, along with the prominent southern part, is apparently noticeable, identifying the CME as a halo structure. The CME was not seen to be associated with solar flares and radio bursts. The observed CME morphology was fitted with a graduated cylindrical shell (GCS; A. Thernisien et al. 2009) model. This delineates the CME as a halo structure, although it is seen mostly in the south as a narrow structure. The underlying FR at a latitude of $-37°$ with a tilt angle of $-80°$, and height of $7.5R_\odot$ better represents the observed CME morphology (middle panels) at 23:00 UT. If the latitude is near zero, then the CME might have emerged symmetrically in the south and north parts of the solar disk. This CME FR expanded to 20.7 $R_\odot$ by 20/03:57 UT.

On visually examining the regular EUV images 4 hr prior to the CME appearance in LASCO/C2, it was found that, surprisingly, this CME was not linked to any apparent LCS such as flare ribbons, EUV dimming, or posteruption arcades. Due to weak or unnoticeable low coronal characteristics, this CME falls in the category of stealth CME directed toward the Earth.

To determine the source region of the CME, we analyze the EUV imaging observations obtained from SDO/Atmospheric Imaging Assembly (AIA) and STA/EUVI. AIA captures the full disk of the Sun in 10 different wavelengths with a cadence of 12 s (J. R. Lemen et al. 2012). Figures 4(a)–(b) present full-disk observations of the Sun in AIA 193 and 211 Å wavelength channels taken 4 hr prior to the emergence of the CME in LASCO/C2. These images reveal a longitudinal filament channel extending across the equator, along with an S-shaped filament in the southern region. Notably, these features are absent in the AIA 304 Å observations, suggesting that the plasma in the filament channel is diffuse. The filament channel measures approximately 1000″ longitudinally and slightly over 200″ laterally, appearing as an uneven longitudinal strip that is dimmer than the surrounding quiet regions of the Sun. Additionally, a huge coronal hole exists in its vicinity to the southeast. The magnetic field distribution observed (Panel 4(c)) indicates that the filament channel formed amidst weak opposite polarities, with positive polarity on the western side and negative polarity on the eastern side of the channel. For the axial field to be directed southward, the helicity

---

[3] https://cdaw.gsfc.nasa.gov/CME_list/

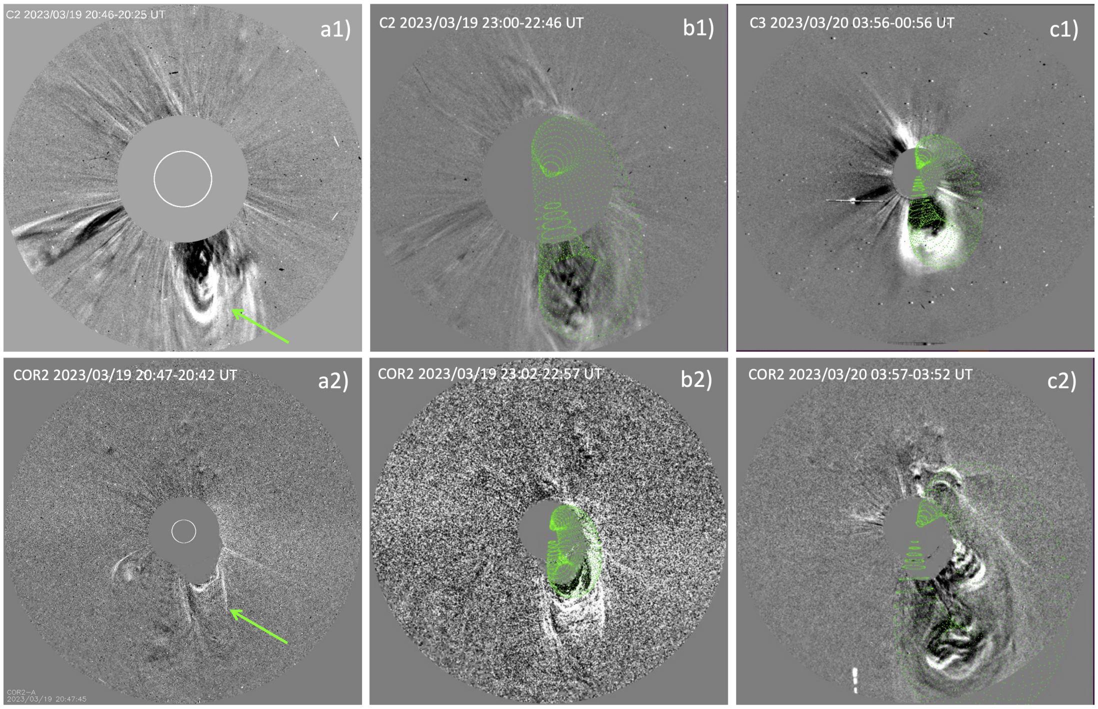

Figure 3. Running difference images of coronagraph observations from SOHO/LASCO and STA/COR2. The southern part of the CME from the eruption of the longitudinal filament channel is visible with a bright LE and the core. GCS fit (green wired) to the CME morphology is overlaid.

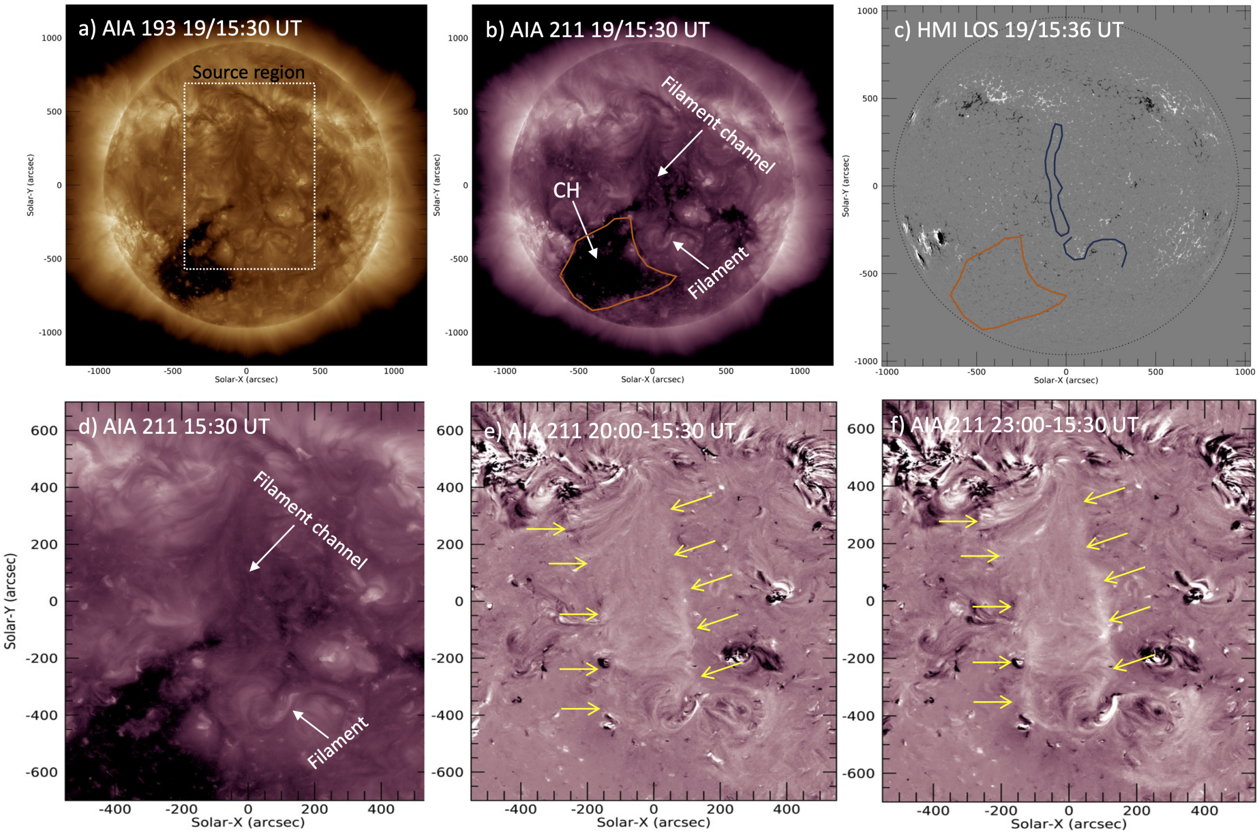

Figure 4. Source region observations of the CME (a) Image of the Sun at 19/15:30 UT in AIA 193 Å channel. The rectangular box encapsulates the source region containing a long transequatorial filament channel and a separate S-shaped filament that are being erupted at a later time. (b) Sun in AIA 211 Å wavelength. The coronal hole, along with the filaments, is referred to with the arrows. (c) HMI magnetogram showing the magnetic field distribution at the photosphere. To identify the location, the filaments and coronal hole are roughly sketched over the magnetogram. (d) Source region in AIA 211 Å. (e)–(f) Base difference images showing faint bright channels (pointed with yellow arrows) along the extent of filaments being erupted.

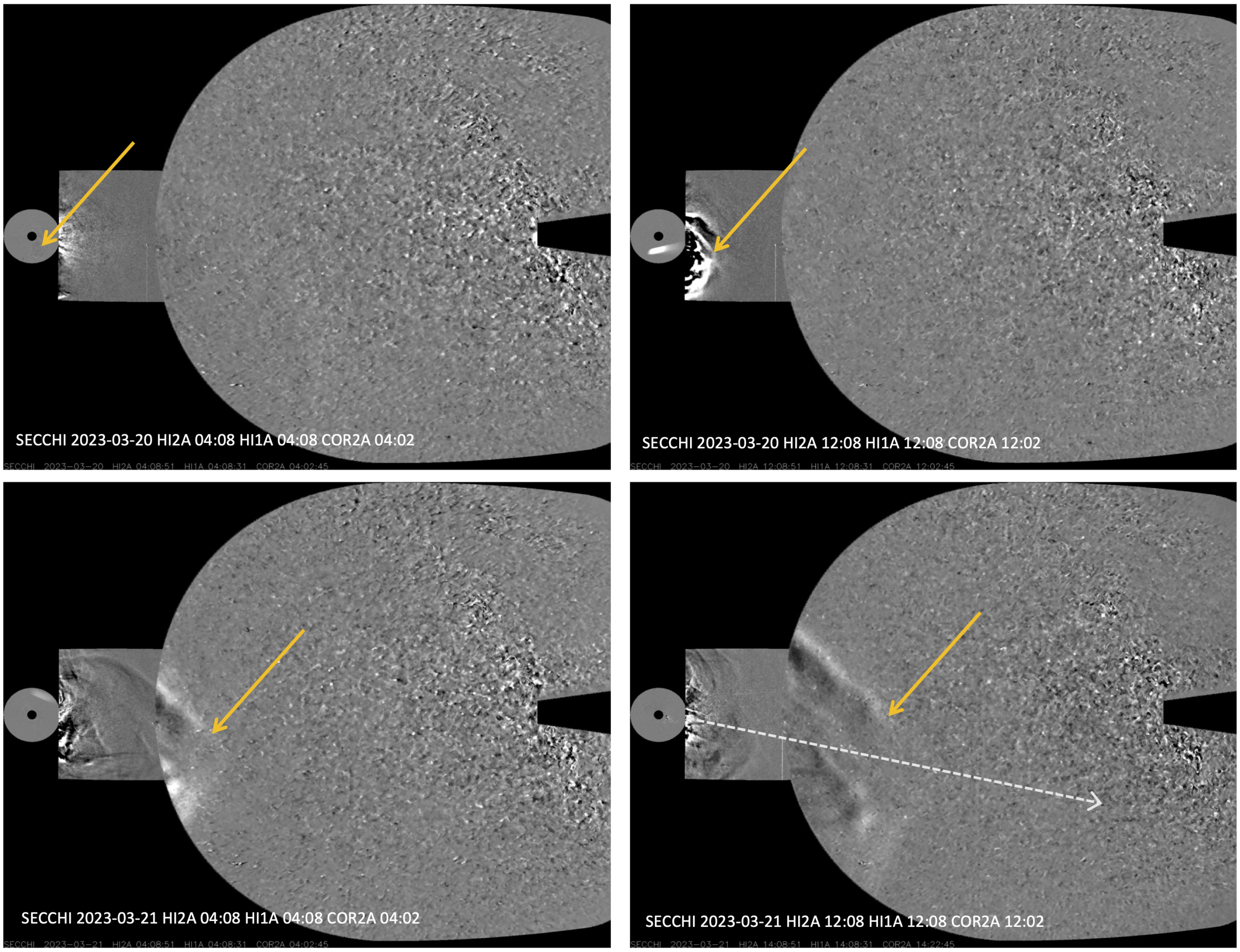

Figure 5. CME propagation from the low corona into the heliosphere. Panels show the combined images prepared from running difference images of STA/COR2, STA/HI1, and STA/HI2. The yellow dotted arrows point to the CME's leading edge at different epochs during March 20–21. White-dashed arrow indicates the slit position to construct the J-map. Due to the low separation angle (12°) of STA with the Sun–Earth line, these images capture the CME propagation with projection effects.

must be right-handed, as observed in situ; however, the threads within the channel are not sufficiently pronounced to support this. Minimal emissive activity was detected within the channel between March 18 and 19, and standard EUV observations provided inconclusive results regarding any eruptive signatures. To investigate its connection to the observed CME, we analyzed the EUV images by applying various combinations of differencing cadence. We utilized the base image taken at 15:30 UT, as shown in Figure 4(d), to subtract from the images captured until the CME observation time in LASCO/C2. Before subtraction, the images are corrected for solar rotation.

Figures 4(e)–(f) display the base difference maps of the source region, capturing the faint brightening along the extent of the channel starting from 18:00 UT and becoming more pronounced after 20:00 UT on March 19. We speculate that the reconnection processes may have created a magnetic structure without filament material that was slowly expelled from the Sun, and this structure may have contributed to a CME formation. As a result, the posteruption arcades form due to reconnection underneath the erupting FR (filament). The observed faint brightening along the filament channel over the course of 4 hr suggests that the eruption is slow, such that the channel smoothly transitioned to a CME. A slight transverse expansion within the channel was also noted. The laterally formed posteruption arcades and brightenings suggested the presence of a longitudinal FR configuration. These coronal signatures observed between 20:00 UT and 23:00 UT on March 19 indicated a slow and subtle eruption of the longitudinal filament channel, resulting in a CME. This narrow longitudinal filament channel resembled the shape and morphology of the CME, as also delineated by the GCS fit, confirming that the LCS observed above corresponded to the CME. Because of the slow eruption, the CME has a low linear speed of around 300 km s^{-1}, and underwent slow acceleration during its early phase. A detailed study by W. Teng et al. (2024) reveals that this storm on 2023 March 23 was indeed associated with the eruption of a longitudinal (transequatorial) filament channel on March 19, exhibiting weak LCS and faint CME emission. In Sections 4 and 5, we will provide a detailed analysis of the CME's heliospheric propagation and its in situ observations at varying radial distances.

4. Heliospheric Propagation of the CME

The CME's heliospheric propagation was further tracked using the wide-angle observations from the Heliospheric Imagers (HI1 and HI2) on board the STA. The RD images from each instrument's observations were combined to create composite images that visualized the CME's lateral expansion as it radially propagates. Figure 5 shows the composite images at four selected epochs. Visibly, the CME exhibited asymmetrical

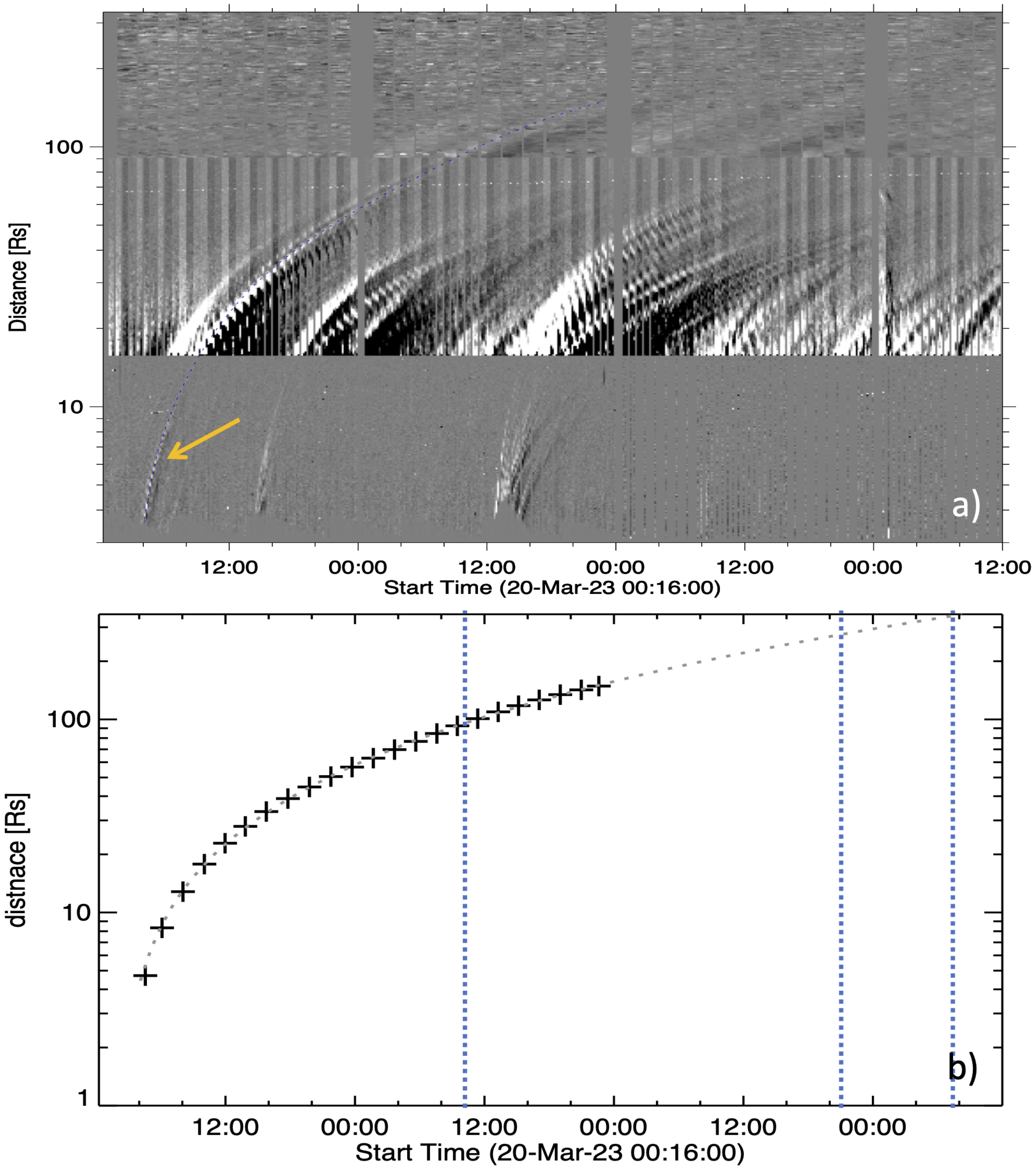

Figure 6. (a) The time-elongation map (J-map). The blue-dotted curve along the bright streak represents traces of the CME trajectory. (b) The height–time plot derived from the J-map. The "+" symbols are the plotted points from the J-map. The dotted curve is the second-order polynomial fit. The vertical dotted lines refer to in situ arrival ICME at SolO (21/09:20 UT), STA (22/21:20 UT), and WIND (23/07:30 UT), respectively.

expansion in the plane of the sky, as we can observe the distorted LE and the southward part advancing faster than the northward LE segment in the HI2 field of view (FOV; Figures 5(c)–(d)). Using these composite images, the LE of the CME was tracked, where its transit was along the position angle of 250°. The resulting J-map is displayed in Figure 6. In the J-map, the CME-LE is identified as a bright streak, which is traced by a blue-dotted line. As the CME moves farther away from the Sun, it becomes diffused, and the LE is traceable only up to 130 $R_\odot$. We have fitted the height–time information obtained from this J-map with a second-order polynomial. The ICME arrival time detected by SolO is consistent with the LE propagated to $\approx 100 R_\odot$ in HI. However, the height values corresponding to the ICME arrival at STA and WIND were 240 $R_\odot$ and 320 $R_\odot$, which were inconsistent due to the plane-of-sky projection effects by the halo (I)CME.

From the height–time curve, the CME kinematics are evaluated. In the STA/COR2 FOV, the velocity profile was noted between 00:43 UT and 03:43 UT on 20 March. Between 8.15 $R_\odot$ and 13 $R_\odot$, the velocity of the CME increased from $235.21 \rightarrow 276 \rightarrow 450\,\mathrm{km\,s^{-1}}$. The average velocity was $273\,\mathrm{km\,s^{-1}}$ and its acceleration was $2\,\mathrm{m\,s^{-2}}$. For an extremely slow-moving CME, its acceleration was less and was consistent with the values (-50 to $50\,\mathrm{m\,s^{-2}}$) in the study of N. Gopalswamy (2011). In the HI1 FOV, at 10:00 UT (18 $R_\odot$), 19:46 UT (44.6 $R_\odot$), and 23:04 UT (54.5 R_s) on March 20, the velocities increased from $513.5 \rightarrow 552 \rightarrow 625.5\,\mathrm{km\,s^{-1}}$. The average velocity was $583.3\,\mathrm{km\,s^{-1}}$ with an average

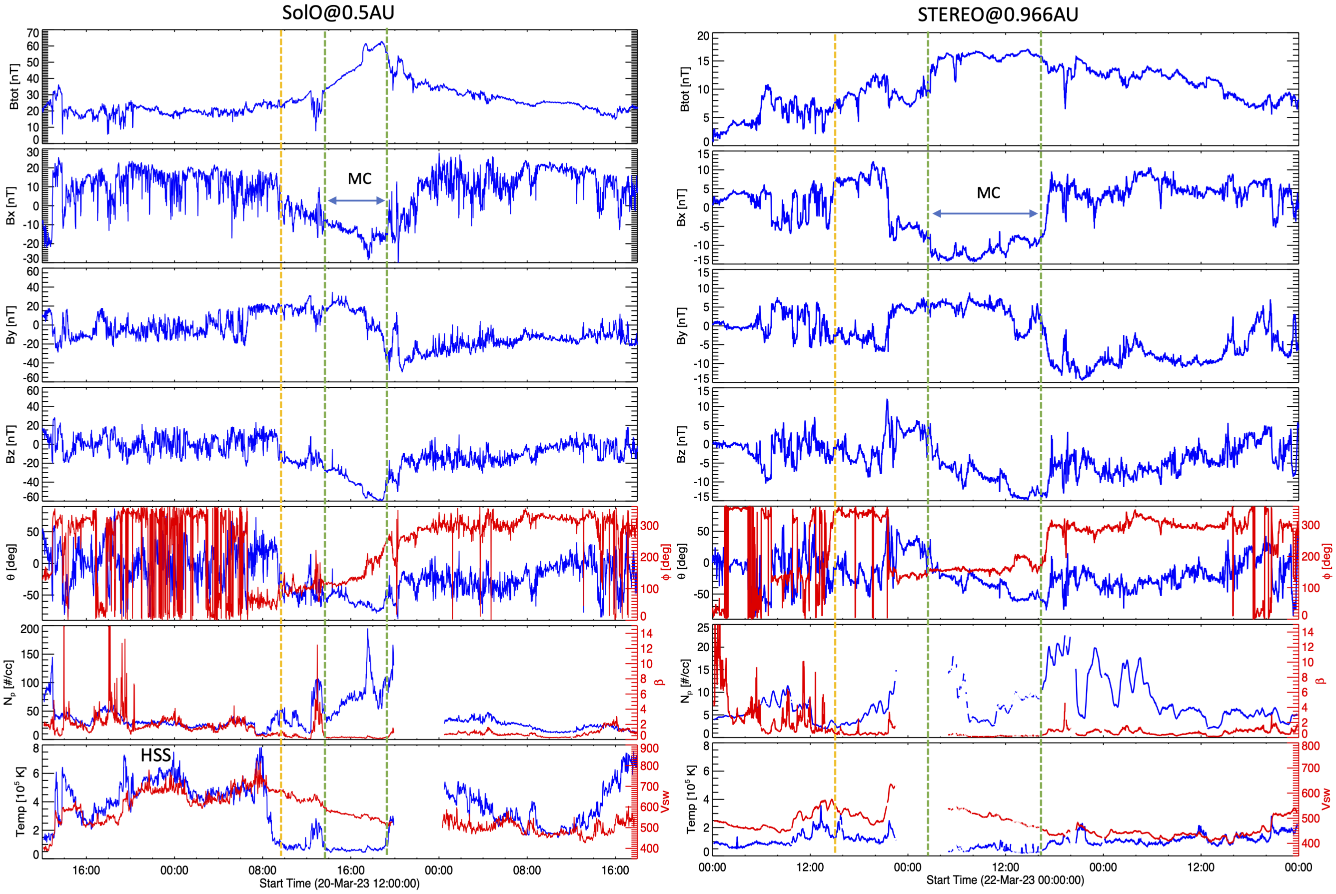

Figure 7. Magnetic and plasma measurements at the SolO, situated at a radial distance of 0.5 au, and the STA located at 0.966 au from the Sun. The panels show, from top to bottom, the total magnetic field; the *X*-, *Y*-, and *Z*-components of the magnetic field in GSE coordinates; the longitude and latitude of the magnetic field angle; the proton density, β; and the temperature and velocity. The orange vertical dashed line refers to ICME arrival, and the green vertical lines refer to the leading and trailing edges of the MC. Data gaps are present with velocity and density measurements in both spacecraft.

acceleration of 3.2 m s^{-2} where both profiles slightly increased. Finally, in the STA/HI2 FOV, between 08:51 UT (90 $R_\odot$) and 15:09 UT (118 $R_\odot$) on 21 March, the velocities further increased to 776–866 km s^{-1}. But the speed of the ICME decreased to 786–773.3 km s^{-1} after 18:22 UT (post 131.5 $R_\odot$). The above velocity estimates are after fitting to the height–time curve and have an uncertainty of up to 5 km s^{-1} as there could be uncertainty in tracing LE. From these kinematic properties, it is evident that the slow CME from the Sun was carried away by the solar wind (P. J. Cargill 2004) with an average velocity of 640 km s^{-1} and an average acceleration of 1.84 m s^{-2} in the heliosphere.

5. In Situ Observations from SolO, STEREO, and WIND

The in situ magnetic field and plasma parameters are measured by the magnetometer (MAG; T. S. Horbury et al. 2020) instrument on board SolO, the IMPACT (J. G. Luhmann et al. 2008), and PLASTIC (A. B. Galvin et al. 2008) instruments on STA, and the MFI (R. P. Lepping et al. 1995) and SWA (K. W. Ogilvie et al. 1995) instruments on board the WIND spacecraft. For ease of understanding, the magnetic field measurements provided in radial, tangential, and normal (RTN) coordinate systems are approximated to the Geocentric Solar Ecliptic (GSE) coordinate system via $B_x \rightarrow -B_R$, $B_y \rightarrow -B_T$, $B_z \rightarrow B_N$. Figure 7 plots the magnetic and plasma measurements by SolO at 0.5 au heliocentric distance in comparison with STA at 0.96 au heliocentric distance.

A high-speed solar wind at an average speed of 680 km s^{-1} passes the SolO from 20:00 UT on March 20, followed by the ICME structure. The same high-speed wind, presumed to have originated from the large coronal hole (See Figure 4), was later observed in WIND from the middle of March 21. The ICME appears to have been encountered at 21/09:20 UT in SolO, with an increased solar wind speed and temperature. The ICME arrival is not noticed with a clear sheath region, but rather a gradual increase of $B_{\rm tot}$ from the background value of 20 nT, and without enhanced proton density. The ICME structure hits the STA at 22/21:20 UT, with an enhanced density, temperature, and velocity. In both of these observations, no signatures of shock presence are noticed, probably due to a slow CME carried by faster solar wind. The pre-ICME wind velocity decreases from 650 km s^{-1} at 0.5 au to 570 km s^{-1} at 0.96 au. In the WIND observations at 1 au, the $V_{\rm sw}$ decreases further to 540 km s^{-1}, which may possibly be related to both radial and longitudinal evolution from STA.

Considering an average wind (CME transit) velocity of 650 km s^{-1} near the Sun (20 $R_\odot$) at 20/02:00 UT, a transit time of 31 hr is consistent with hitting SolO at 21/09:20 UT. This velocity is also in agreement with the observed one in the HI FOV. A transit velocity of 570 km s^{-1} as observed in STA in situ measurements is justifiable for the CME to travel from

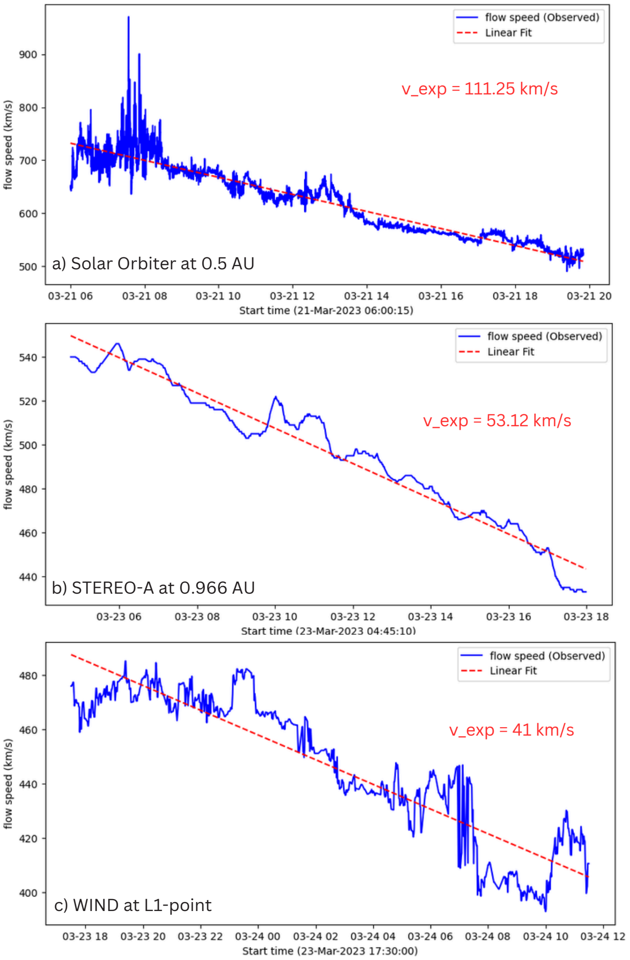

Figure 8. The solar wind velocity during the MC interval was observed at three different heliocentric distances by the SolO, STA, and WIND spacecraft. The red straight line is a linear fit, and the derived expansion speeds are annotated in each panel.

SolO to STA in a duration of 36 hr. From the WIND perspective, a transit time of 77 hr is in reasonable agreement with the observed pre-ICME solar wind velocity of 540 km s^{-1}.

From the ICME arrival at the spacecraft, a low variation of magnetic field components distinct from the background field can be noticed. The variations of the magnetic field are comparable in each component, which is an indication that the same ICME structure passes through the two spacecraft at 0.5 and 0.96 au. According to the criteria for MC structure, its boundary is defined between 13:30 and 19:30 UT on March 21 in SolO/MAG observations and 02:30–17:00 UT on March 23 in STA/IMPACT measurements. The proton density is higher than the background during these intervals, but the proton β is quite small for the MC definition. Consistent with the WIND (See Figure 1) measurements, the density enhancement toward the trailing edge of the MC is also recorded at both SolO and STA spacecraft.

Within the MC FR, the speed drops from 620 to 525 km s^{-1} at SolO and from 580 to 430 km s^{-1} at STA, indicating the expanding MC structure as it moves past the spacecraft. Using the midpoint velocity, the radial width of the MC FR is calculated by multiplying the time duration by the midpoint velocity. In SolO, it is determined to be 0.08 au, which changed by about a factor of 2 to a size of 0.18 au at STA. Due to the longitudinal separation, the MC size observed at WIND is 0.15 au, which is smaller than the size recorded at STA.

The MC's expansion speed ($V_{\rm exp}$) is determined using the velocities at the leading and trailing edges as $V_{\rm exp} = V_{\rm leading} - V_{\rm trailing}$. To achieve this, the velocity during the MC duration is linearly fitted, as depicted in Figure 8, and the slope is taken as the $V_{\rm exp}$. The computed $V_{\rm exp}$ is shown in the corresponding panel. Significantly, the $V_{\rm exp}$ recorded by SolO is 111.25 km s^{-1}, which decreases to approximately 50% at the STA and WIND. A small discrepancy is noted for STA and WIND measurements of $V_{\rm exp}$ (53.12 and 41.0 km s^{-1}), likely arising from their positions accessing different regions of the ICME FR. These velocities align with the computed radial width of the MC FR as it propagates along the Sun–Earth line.

At a small radial separation of 0.02 au, Figure 9 presents a comparison of in situ measurements from STA with WIND. A significant distinction in these measurements lies in the arrival of the ICME. The ICME meets the STA at 22/21:20 UT and the WIND at 23/07:30 UT. A time difference of 21 hr is clearly evident in the arrival of the MC structure at STA and WIND when we examine the Bx-component. We attribute this variation to the corotation time between STA and WIND positions (N. Lugaz et al. 2022). With a corotation rate of $14^{\circ}\!.5$ per day, the 12° longitudinal separation between STA and WIND aligns with the recorded time difference in ICME transit. Besides that, there is a significant resemblance between the Bx-component and the other magnetic field components observed by both spacecraft. In STA, the Bz-component becomes more negative from the leading to the trailing edge, while in WIND measurements exhibit an opposite behavior, possibly due to the spacecraft passing away from the MC's center. Unlike STA, the magnetic field components are compressed in front of MC in the WIND due to the high-speed stream. Additionally, the magnetic field strength $B_{\rm tot}$ peaked at approximately $\sim$20.76 and $\sim$17.01 nT during the MC interval for the WIND and STA, respectively. These values relate to a power law indicating a decrease in magnetic field with increasing heliocentric distance $B_{\rm peak} \propto R_H^{-2.1}$ from SolO to STA, and a power law of $B_{\rm peak} \propto R_H^{-1.7}$ from SolO to WIND. For the average MC field strength, these relations hold with a slight variation as $B_{av} \propto R_H^{-1.97}$ and $B_{av} \propto R_H^{-1.53}$, respectively.

In the MC structure presented in Figure 7, the By-component changes from positive to negative, while the Bz-component stays negative in SolO. This led to the elevation angle (θ) of the magnetic vector becoming more inclined toward the south relative to the ecliptic plane, with the azimuthal angle (ϕ) changing from 90° to 210° in SolO. The noted evolution in θ and ϕ indicates that the MC structure possesses an ESW magnetic configuration characterized by right-handed helicity. Unlike SoLO, the By-component stays positive, while the Bz-component varies from positive to negative at STA, causing the magnetic vector to become more southward as ϕ rotates near 140° (east). In this case, the magnetic structure within the MC FR is identified as an ESW (east-southwest) configuration with right-handed helicity (V. Bothmer & R. Schwenn 1998).

For the orientation of the MC FR, we employed minimum variance analysis (MVA; B. U. O. Sonnerup & L. J. Cahill 1967; V. Bothmer & R. Schwenn 1998), which involves calculating the covariance matrix of the magnetic field components and their eigenvectors. The eigenvector corresponding to the intermediate

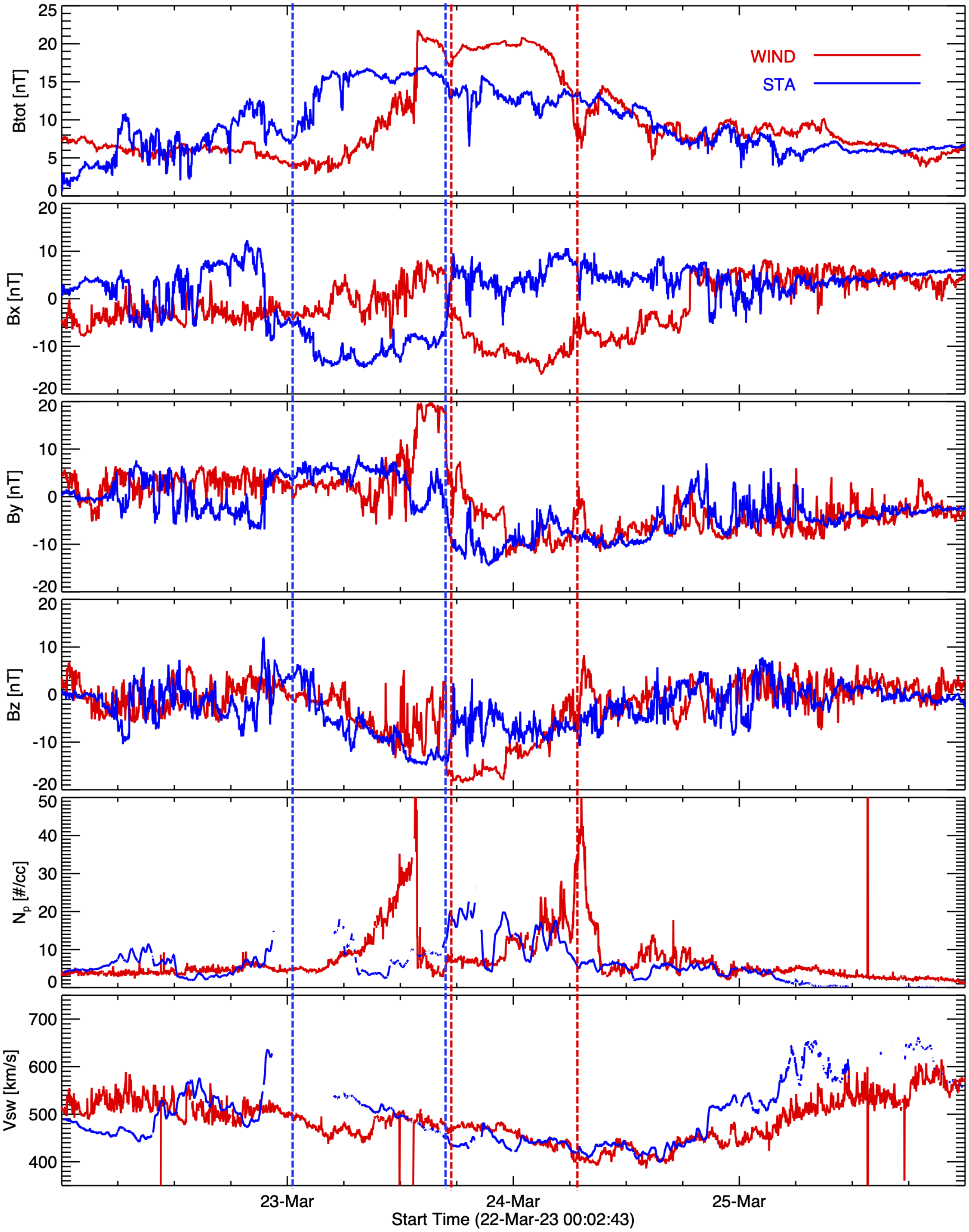

Figure 9. Comparison of solar wind measurements at STA (blue) and WIND (red). The MC interval is marked with vertical dotted lines.

variance direction gives the orientation of the MC axis (H. Goldstein 1983). Although the variations of magnetic fields are similar due to the radial lineup of the spacecraft, the inclination of the MC axis is found to decrease from $\theta = -69°$ at SolO to $\theta = -25°$ at STA with respect to the ecliptic plane. For comparison, this inclination of the MC axis seen by SolO differs by 20° with respect to the orientation of the filament channel in the solar source region, which is longitudinal with a southward axial field. This decrease in the inclination is a clear signature of the rotation of the MC axis during its radial propagation. Further, even at close radial separation (0.02 au), a difference in axis inclination $\delta\theta = 10°$ is noticed between WIND and STA. The different characteristics of ICME seen by spacecraft are compiled in Table 1.

Table 1
Characteristics of the ICME Observed by Three Different Spacecraft

Property	SolO (0.5 au)	STEREO-A (0.966 au)	WIND (L1; 0.99 au)
ICME encounter	21/09:20 UT	22/21:20 UT	23/07:30 UT
MC interval	21/13:30–19:30 UT	23/02:30–17:00 UT	23/18:00–24/07:30 UT
Velocity at mid of MC	560 km s^{-1}	505 km s^{-1}	470 km s^{-1}
Expansion speed	111 km s^{-1}	50 km s^{-1}	40 km s^{-1}
MC radial size	0.08 au	0.18 au	0.15 au
Peak $B_{\rm tot}$	62.78 nT	17.01 nT	20.76 nT
mean($B_{\rm tot}$) in MC	48.2 nT	14.2 nT	18.0 nT
MC type	ESW	ESW	SWN
MC magnetic helicity	Right-handed	Right-handed	Right-handed
MVA orientation (θ, ϕ)	$-69\overset{\circ}{.}5$, $-165\overset{\circ}{.}9$	$-25\overset{\circ}{.}1$, $-143\overset{\circ}{.}6$	$-34\overset{\circ}{.}5$, $-254\overset{\circ}{.}2$

6. Summary and Conclusions

We studied the solar origins of an intense geomagnetic storm that occurred on 2023 March 23. There were multiple candidate CMEs for this storm during March 19–21, but they were ruled out due to their position of emergence from the limb. A weak CME observed on March 19, at 18:00 UT was identified as the solar source to cause this geomagnetic storm. This weak CME was linked to the eruption of the longitudinal filament channel present at the center of the solar disk from around 18:00 UT onward, as also studied by W. Teng et al. (2024). The filament channel lies along the PIL of distributed weak opposite polarities with a right-handed magnetic twist and southward axial field. Such structures are ideal candidates for producing geoeffective CMEs. Unlike typical eruptions, this filament channel undergoes a smooth transition to the eruption phase, leaving extremely weak LCS. As a result, the CME is not associated with any flare or radio burst. Because of weak or undetectable LCS, the CME is categorized as a stealthy one and is an addition to the stealth CMEs so far identified for their potential geoeffectiveness (N. V. Nitta et al. 2021).

The heliospheric propagation of the CME was tracked using wide-angle observations from the STA's Heliospheric Imagers. Combined images revealed the CME's asymmetric lateral expansion, with the southern LE advancing faster than the northern segment. The LE was tracked along a position angle of 250°, and a J-map traced its motion up to 130 $R_\odot$, showing diffusion with increasing distance. From the height–time data extracted from the J-map, it is inferred that the CME's arrival at SolO matched the propagation seen in HI. Overall, the slow CME was accelerated by the solar wind drag, achieving an average heliospheric velocity of 640 km s^{-1} and an acceleration of 1.84 m s^{-2}.

Further, the radial evolution of the ICME is examined utilizing in situ observations from spacecraft in close radial alignment. The ICME, preceded by a high-speed solar wind (680 km s^{-1}), was detected without a clear shock or sheath. The ICME's arrival times and propagation speeds were consistent across spacecraft: SolO (0.5 au) at 21/09:20 UT, STA (0.96 au) at 22/21:20 UT, and WIND (0.99 au) at 23/07:30 UT. A 21 hr time lag in ICME arrival between STA and WIND is attributed to a 12° longitudinal separation and solar rotation. The ICME's field component variations are comparable from each spacecraft, with MC signatures suggesting the same ICME structure was encountered. The MC interval observed in all spacecraft shows a decreasing velocity (indicating expansion), a growing radial size (from 0.08 au at SolO to 0.18 au at STA), and a reduction in expansion speed—from 111.25 km s^{-1} at SolO to about half of that at STA and WIND. A power-law relation describes the observed decrease in magnetic field strength with heliocentric distance, with $B_{\rm peak} \propto R_H^{-2.1}$ (SolO–STA) and $B_{\rm peak} \propto R_H^{-1.7}$ (SolO–WIND).

MC's radial evolution is observed with differences in B_z behavior, which is increasing at STA and decreasing at WIND. The MC magnetic structure is with ESW configuration at SolO and STA, whereas it is with SWN configuration at WIND, all of which implies a right-handed magnetic helicity consistent with the source region. The MVA indicates that the MC axis is directed at –69° at SolO, closely aligning with the longitudinal filament channel in the source region. However, the inclination of the MC axis is reduced to −25° at STA and −34° at WIND with respect to the ecliptic, indicating the rotation during MC's propagation in the heliosphere. In summary, the findings emphasize the dynamic expansion, rotation, and structural evolution of the ICME as it propagates through the inner heliosphere.

The Dst index that is observed can be represented by an empirical formula relating the solar wind parameters to the intensity of geomagnetic storms. Commonly used empirical models are R. K. Burton et al. (1975) and T. P. O'Brien & R. L. McPherron (2000) (BM, OM, hereafter) that are based on the assumption that the ring current injection is a linear function of the solar wind's dawn-to-dusk electric field (E_y). C. B. Wang et al. (2003; WM hereafter) used an empirical equation providing enhanced Dst estimates, which incorporates the injection term of the ring current based on both the solar wind electric field and the dynamic pressure ($P_{\rm dyn} = nV_{\rm sw}^2$). Figure 10(a)–(b) shows the $P_{\rm dyn}$ and E_y as a function of time. The observed (SYM-H) and estimated Dst are plotted in Figure 10(c). During the sheath interval, the $P_{\rm dyn}$ reached a maximum of 13 nPa, and E_y peaked at 5 mV m^{-1}, correlating with a SYM-H peak of –67 nT at 23/14:45 UT. Owing to the southward Bz, the electric field E_y maintained a high value of 8 mV m^{-1} in the first 6 hr of the MC interval, followed by a steep decline toward the MC tail. In contrast, due to density enhancement toward the MC tail, the $P_{\rm dyn}$ increases from 2 to 8 nPa. The storm's main phase is driven primarily by E_y, however, its steep decline later is compensated by the density enhancement from 23/23:00 UT to sustain and further drive the storm until 24/06:00 UT. The main phase of the storm leads to a peak intensity of SYM-H = −169 nT occurring at 24/02:40 UT. The role of density enhancement is clearly indicated by the second peak of SYM-H = −170 nT at

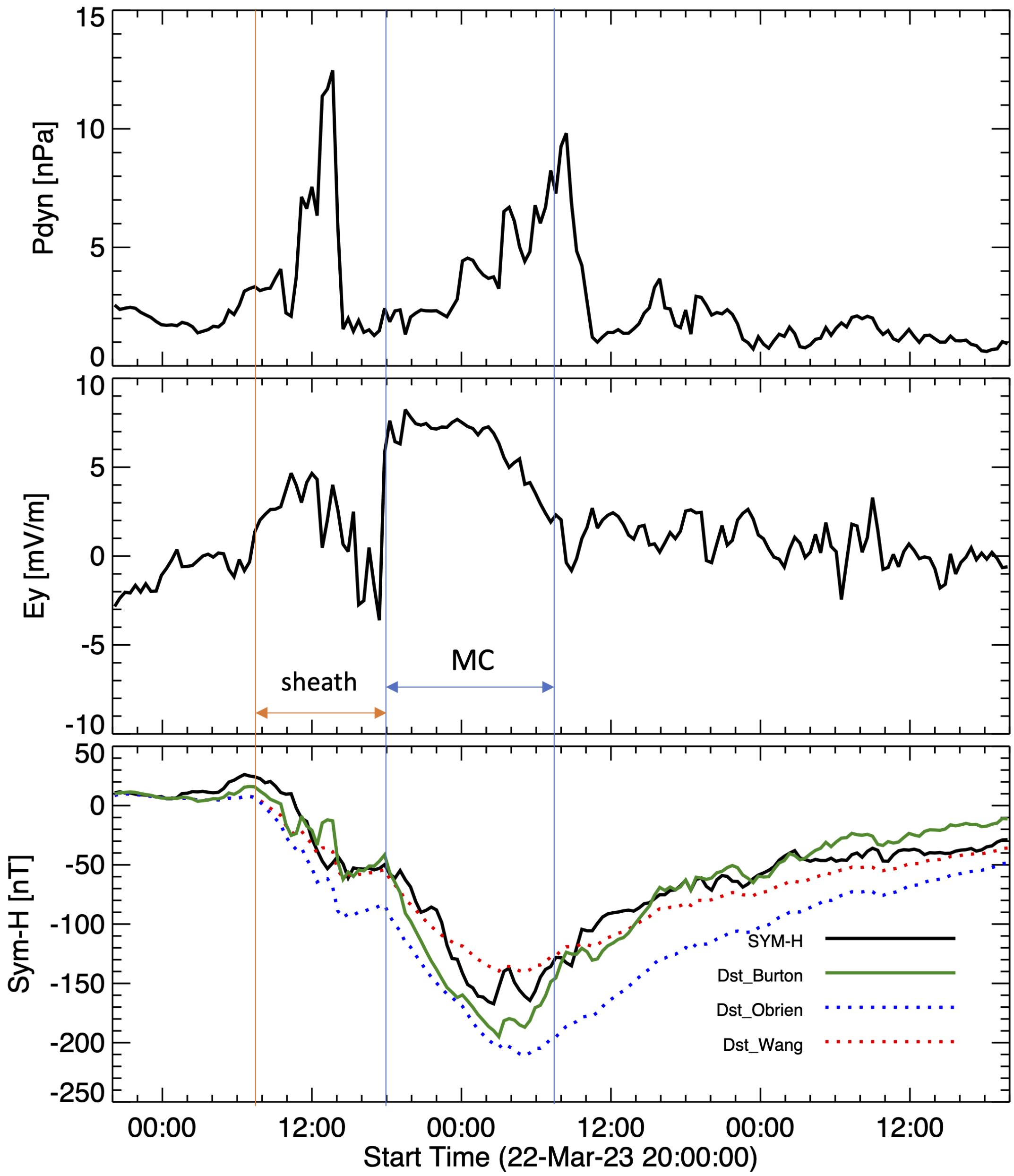

Figure 10. Solar wind dynamic pressure (top), electric field (middle), and observed Dst index (bottom) as a function of time. Estimated Dst index with the models by R. K. Burton et al. (1975), T. P. O'Brien & R. L. McPherron (2000), and C. B. Wang et al. (2003) are overplotted.

24/05:20 UT. MC structures with enhanced density are suggested to cause intense storms; for example, the 2018 August 26 storm has a steepening Dst profile coincident precisely with the increase of density from 02:00 UT in the MC interval (N. Gopalswamy et al. 2022). Empirical models assess the initial, main, and recovery phases of the storm quite effectively, yielding root mean square errors of 18.1, 40.7, and 14.1 nT, respectively, for BM, OM, and WM. The BM overestimates the SYM-H with a peak intensity of −196 nT, while the WM underestimates the storm's peak strength at −152 nT. By incorporating P_{dyn} into the empirical formula, the WM more closely matches the observed Dst, while the BM also achieves a comparable Dst profile by reproducing the two peaks. Our study reports a unique CME that is inconspicuous near the Sun, propagates to the near-Earth environment with southward Bz and enhanced density, together causing intense geomagnetic activity.

Acknowledgments

SDO is a mission of NASA's Living With a Star Program; STEREO is the third mission in NASA's Solar Terrestrial Probes program; and SOHO is a mission of international cooperation between the ESA and NASA. We acknowledge the use of NASA/GSFC's Space Physics Data Facility's OMNIWeb (or CDAWeb or ftp) service. The CME catalog used in this study is generated and maintained by the Center for Solar Physics and Space Weather, the Catholic University of America, in cooperation with the Naval Research Laboratory and NASA. The authors thank the reviewer for detailed constructive comments and suggestions that helped improve the presentation of the analysis.

ORCID iDs

P. Vemareddy https://orcid.org/0000-0003-4433-8823
K. Selva Bharathi https://orcid.org/0009-0006-7652-9754

References

Alzate, N., & Morgan, H. 2017, ApJ, 840, 103
Belakhovsky, V. B., Vasilev, A. E., Kalishin, A. S., & Roldugin, A. V. 2024, BRASP, 88, 359
Bisoi, S. K., Chakrabarty, D., Janardhan, P., et al. 2016, JGRA, 121, 3882
Bothmer, V., & Schwenn, R. 1998, AnGeo, 16, 1
Brueckner, G. E., Howard, R. A., Koomen, M. J., et al. 1995, SoPh, 162, 357
Burton, R. K., McPherron, R. L., & Russell, C. T. 1975, JGR, 80, 4204
Canfield, R. C., Hudson, H. S., & McKenzie, D. E. 1999, GeoRL, 26, 627
Cargill, P. J. 2004, SoPh, 221, 135
Cheng, X., Zhang, J., Ding, M. D., et al. 2013, ApJL, 769, L25
Davies, E. E., Forsyth, R. J., Good, S. W., & Kilpua, E. K. J. 2020, SoPh, 295, 157
Davies, E. E., Möstl, C., Owens, M. J., et al. 2021, A&A, 656, A2
Fenrich, F. R., & Luhmann, J. G. 1998, GeoRL, 25, 2999
Galvin, A. B., Kistler, L. M., Popecki, M. A., et al. 2008, SSRv, 136, 437
Goldstein, H. 1983, in NASA Conf. Publication, Vol. 228, ed. M. Neugebauer (Washington, DC: NASA), 731
Gonzalez, W. D., Joselyn, J.-A., Kamide, Y., et al. 1994, JGRA, 99, 5771
Gonzalez, W. D., Tsurutani, B. T., & Clúa de Gonzalez, A. L. 1999, SSRv, 88, 529
Gopalswamy, N. 2011, in Astronomical Society of India Conf. Ser. 2, 241
Gopalswamy, N., Shimojo, M., Lu, W., et al. 2003, ApJ, 586, 562
Gopalswamy, N., Yashiro, S., Akiyama, S., et al. 2022, JGRA, 127, e30404
Gopalswamy, N., Yashiro, S., Krucker, S., & Howard, R. A. 2005, in IAU Symp. 226, Coronal and Stellar Mass Ejections, ed. K. Dere, J. Wang, & Y. Yan (Cambridge: Cambridge Univ. Press), 367
Gosling, J. T., McComas, D. J., Phillips, J. L., & Bame, S. J. 1991, JGR, 96, 7831
Horbury, T. S., O'Brien, H., Carrasco Blazquez, I., et al. 2020, A&A, 642, A9
Howard, R. A., Michels, D. J., Sheeley, N. R., Jr., & Koomen, M. J. 1982, ApJ, 263, L101
Kaiser, M. L., Kucera, T. A., Davila, J. M., et al. 2008, SSRv, 136, 5
Lemen, J. R., Title, A. M., Akin, D. J., et al. 2012, SoPh, 275, 17
Lepping, R. P., Acũna, M. H., Burlaga, L. F., et al. 1995, SSRv, 71, 207
Lugaz, N., Salman, T. M., Zhuang, B., et al. 2022, ApJ, 929, 149
Luhmann, J. G., Curtis, D. W., Schroeder, P., et al. 2008, SSRv, 136, 117
Möstl, C., Weiss, A. J., Reiss, M. A., et al. 2022, ApJL, 924, L6
Mulligan, T., Russell, C. T., & Luhmann, J. G. 1998, GeoRL, 25, 2959
Nitta, N. V., & Mulligan, T. 2017, SoPh, 292, 125
Nitta, N. V., Mulligan, T., Kilpua, E. K. J., et al. 2021, SSRv, 217, 82
Nykiel, G., Ferreira, A., Günzkofer, F., et al. 2024, JGRA, 129, e2023JA032145
O'Brien, T. P., & McPherron, R. L. 2000, JGR, 105, 7707
Ogilvie, K. W., Chornay, D. J., Fritzenreiter, R. J., et al. 1995, SSRv, 71, 55
O'Kane, J., Green, L. M., Davies, E. E., et al. 2021, A&A, 656, L6
Oughton, E. J., Skelton, A., Horne, R. B., Thomson, A. W. P., & Gaunt, C. T. 2017, SpWea, 15, 65
Pesnell, W. D., Thompson, B. J., & Chamberlin, P. C. 2012, SoPh, 275, 3
Pevtsov, A. A., Panasenco, O., & Martin, S. F. 2012, SoPh, 277, 185
Richardson, I. G., & Cane, H. V. 2010, SoPh, 264, 189
Robbrecht, E., Patsourakos, S., & Vourlidas, A. 2009, ApJ, 701, 283
Sonnerup, B. U. O., & Cahill, L. J., Jr. 1967, JGR, 72, 171
Teng, W., Su, Y., Ji, H., & Zhang, Q. 2024, NatCo, 15, 9198
Thernisien, A., Vourlidas, A., & Howard, R. A. 2009, SoPh, 256, 111
Vasantharaju, N., Vemareddy, P., Ravindra, B., & Doddamani, V. H. 2019, ApJ, 874, 182
Vemareddy, P. 2024, ApJ, 961, 199
Vemareddy, P., Démoulin, P., Sasikumar Raja, K., et al. 2022, ApJ, 927, 108
Vemareddy, P., Gopalswamy, N., & Ravindra, B. 2017, ApJ, 850, 38
Vemareddy, P., & Ibrahim, M. S. 2024, MNRAS, 527, 1774
Vemareddy, P., Maurya, R. A., & Ambastha, A. 2012, SoPh, 277, 337
Vemareddy, P., & Zhang, J. 2014, ApJ, 797, 80
Wang, C. B., Chao, J. K., & Lin, C. H. 2003, JGRA, 108, 1341
Webb, D. F., & Hundhausen, A. J. 1987, SoPh, 108, 383
Yashiro, S., Gopalswamy, N., Michalek, G., et al. 2004, JGRA, 109, 7105
Zhang, J., Richardson, I. G., Webb, D. F., et al. 2007, JGRA, 112, A10102